Numerical Prediction of Laminar Shock/Shock Interactions in Hypersonic Flow.

Domenic D'Ambrosio
Politecnico di Torino
Dipartimento di Ingegneria Aeronautica e Spaziale
Corso Duca degli Abruzzi, 24 , 10129 Torino, Italy
domenic@athena.polito.it

The results of a series of numerical simulations are presented of experiments conducted at the ONERA Chalais-Meudon Research Center and at the CALSPAN-University at Buffalo Research Center on shock-shock interactions. The flowfield characteristics are described with the aid of the numerical predictions and the computed values of surface pressure and heat transfer are compared with the experimental measurements for purposes of verification and validation. A preliminary grid refinement study is conducted in some test conditions to investigate certain discrepancies that have been found between the numerical and the experimental data.

Nomenclature

Re	Reynolds number per meter, m^{-1}
M	Mach number
ρ	Density, kg/m^3
p	Pressure, Pa
T	Temperature, K
R_{cyl}	Cylinder radius, reference lenght, m
x, y	Cartesian body axes, m

Subscripts

∞	Freestream conditions
w	Wall conditions

Superscripts

o	Stagnation conditions

Introduction

THE correct evaluation of the heat load produced by shock/shock interaction represents an important and critical problem in the design of hypersonic vehicles. It is well known, in fact, that shock/shock interference produces very high levels of heat transfer and surface pressure in the regions of the aircraft that are close to the impinging point. In air-breathing hypersonic vehicles, the phenomenon is typically located at the intake cowl lip, where the shocks produced by the compression ramps intersects the bow shock ahead of the cowl, but it may affect in a similar manner the wing or the fin leading edge also.

In a fundamental work for the study of shock-on-shock interactions, Edney[1] classified six types of flow patterns, which depend on the relative position of the incoming shock with respect to the bow shock. Between them, the so-called type III and type IV interaction are the most critical, since they are characterized by the largest values of wall pressure and heat transfer. In the Edney type III interaction, pressure and heat flux peaks at the wall are related to the impact of the shear layer produced by the shock interference, while in the Edney type IV interaction, even larger loads are due to the impingement of a supersonic jet on the body surface.

In the last years, some experimental campaigns have been conducted with the aim of better understanding the phenomenon and of providing data for code validation. In fact, even though the Computational Fluid Dynamics is widely used today in the prediction of hypersonic flows for design purposes, it is still uncertain whether it can be considered as reliable for simulating any kind of flow, expecially when they present complicated features and different scales. The two most recent sets of experiments on shock/shock interaction were conducted at ONERA Chalais-Meudon (France) in the wind tunnel R5Ch[2] and at the Calspan-University at Buffalo Research Center (CUBRC) (U.S.A.), in the Large Energy National Shock (LENS) tunnel.[3] Subsequently, various numerical simulations have been carried out for reproducing the experimental data, in particular those obtained by ONERA.[4–6] In addition, both the experiments have been selected for validating CFD capability in the framework of the activities of the NATO Research Technology Organization (RTO) Advanced Vehicle Technology (AVT) Working Group 10, Subgroup 3 "CFD Validation for Hypersonic Flight".[7]

In this paper, the results of numerical predictions of both the French and the American experiments will be

Report Documentation Page

Form Approved
OMB No. 0704-0188

1. REPORT DATE	2. REPORT TYPE	3. DATES COVERED
01 JAN 2006	**N/A**	**-**

4. TITLE AND SUBTITLE	5a. CONTRACT NUMBER
Numerical Prediction of Laminar Shock/Shock Interactions in Hypersonic Flow	5b. GRANT NUMBER
	5c. PROGRAM ELEMENT NUMBER
6. AUTHOR(S)	5d. PROJECT NUMBER
	5e. TASK NUMBER
	5f. WORK UNIT NUMBER
7. PERFORMING ORGANIZATION NAME(S) AND ADDRESS(ES) **Dipartimento di Ingegneria Aeronautica e Spaziale Corso Duca degli Abruzzi, 24, 10129 Torino, Italy**	8. PERFORMING ORGANIZATION REPORT NUMBER
9. SPONSORING/MONITORING AGENCY NAME(S) AND ADDRESS(ES)	10. SPONSOR/MONITOR'S ACRONYM(S)
	11. SPONSOR/MONITOR'S REPORT NUMBER(S)

12. DISTRIBUTION/AVAILABILITY STATEMENT
Approved for public release, distribution unlimited

13. SUPPLEMENTARY NOTES
See also ADM001860, Technologies for Propelled Hypersonic Flight (Technologies des vols hypersoniques propulses). , The original document contains color images.

14. ABSTRACT

15. SUBJECT TERMS

16. SECURITY CLASSIFICATION OF:			17. LIMITATION OF ABSTRACT	18. NUMBER OF PAGES	19a. NAME OF RESPONSIBLE PERSON
a. REPORT	b. ABSTRACT	c. THIS PAGE			
unclassified	**unclassified**	**unclassified**	**UU**	**10**	

presented and a validation study will be done.

MODEL SETUP AND TEST CONDITIONS.

The ONERA experiments.[2]

The experiments carried out at ONERA in R5Ch blow-down wind tunnel were characterized by the nominal stagnation and freestream conditions listed in table 1. The experimental set-up that produced the Edney type IV interaction is shown in figure 1. The shock generator, a prism whose cross section is an isosceles triangle with the base 100 mm long and leading edge angle of 10^o, has a spanwise dimension of 100 mm. In the present experiments, it was rotated of 10^o with respect to the freestream, so that a wedge/flat plate configuration with 20^o wedge angle was obtained. The cylinder, which was placed perpendicular to the freestream, has a radius of 8 mm. Since its span is 100 mm wide, a two-dimensional flow could be assumed at the middle of the model, where the measurement equipment was mounted. The relative locations of the cylinder and the wedge could be varied in order to obtain different types of shock-shock interactions. In particular, for the Edney type IV interference, the distance between the leading edge of the shock generator and the cylinder center was 110 mm along the x-axis and 53 mm along the y-axis. Two models of the cylinder were built and equipped with pressure taps and thermocouples to measure surface pressure and heat transfer respectively. In addition, a Dual-line Coherent Anti Stokes Scattering (DL-CARS) technique was used to perform instantaneous measurements of temperature and density inside the flowfield.

Table 1 Experimental conditions at ONERA.

T^o	=	1050	K
p^o	=	250000	Pa
T_∞	=	52.5	K
p_∞	=	5.9	Pa
M_∞	=	9.95	
Re_∞	=	$1.66 \cdot 10^5$	m^{-1}
R_{cyl}	=	0.008	m

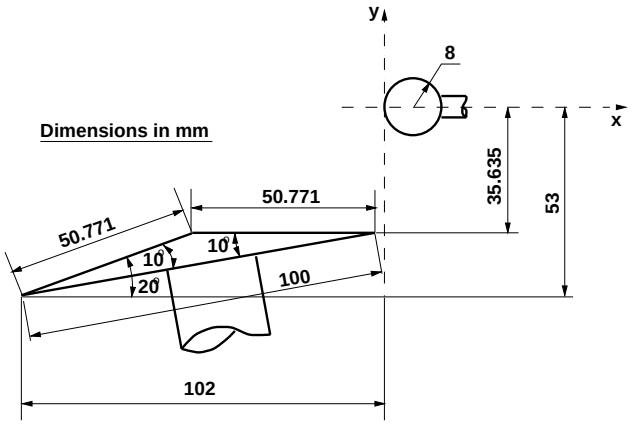

Fig. 1 Model used in the ONERA experiments for the EDNEY type IV interaction

The CALSPAN experiments.[3]

Experimental studies were conducted at CALSPAN in the Veridian 48-inch shock tunnel to obtain detailed heat transfer and pressure measurements in regions of shock/shock interaction in laminar and turbulent low-density flows at Mach numbers from 10 to 16. Seven runs were conducted in the laminar regime, two at Mach 15.7 using a cylinder with radius of 0.375 inches and five at Mach 14 using a cylinder with radius of 1.5 inches. Other seven runs were in the turbulent regime at Mach 10.8, using a cylinder with radius of 1.5 inches. Miniature high frequency instrumentation was used to resolve the large heat transfer gradients and the flow unsteadiness observed in these studies. In order to minimize errors in the heat transfer measurements, which may arise from lateral heat conduction effects inside the model in case of large peak heating values, it was preferred to use models with non-conducting surfaces. Then, in those experiments where the resulting wall temperature rises were important, the surface temperature distribution was tabulated together with the heat transfer rate, so that it could be used in future numerical predictions as a boundary condition.[3] The data obtained in the experimental studies have been incorporated in a database called CUBDAT,[8] which can be accessed by researchers involved in numerical prediction studies. In this paper, numerical results related to the conditions of runs 38 and 43 of the CUBDAT database will be presented.

Table 2 Experimental conditions at CALSPAN for RUN 38 and RUN 43

		RUN 38	RUN 43	
T^o	=	3211.1	3355.6	K
p^o	=	3212957	2992325	Pa
T_∞	=	100.0	110.	K
p_∞	=	3.66	3.51	Pa
ρ_∞	=	$1.273 \cdot 10^{-4}$	$1.108 \cdot 10^{-4}$	kg/m^3
M_∞	=	14.15	13.94	
Re_∞	=	52165	42618	m^{-1}
T_w	=	296.67	300.	K
R_{cyl}	=	0.0381	0.0381	m

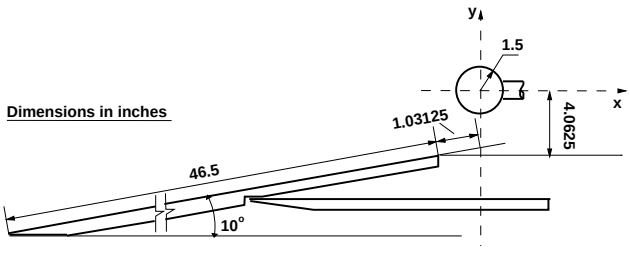

Fig. 2 Model used in the CALSPAN experiments for the EDNEY type IV interaction. RUN 38.

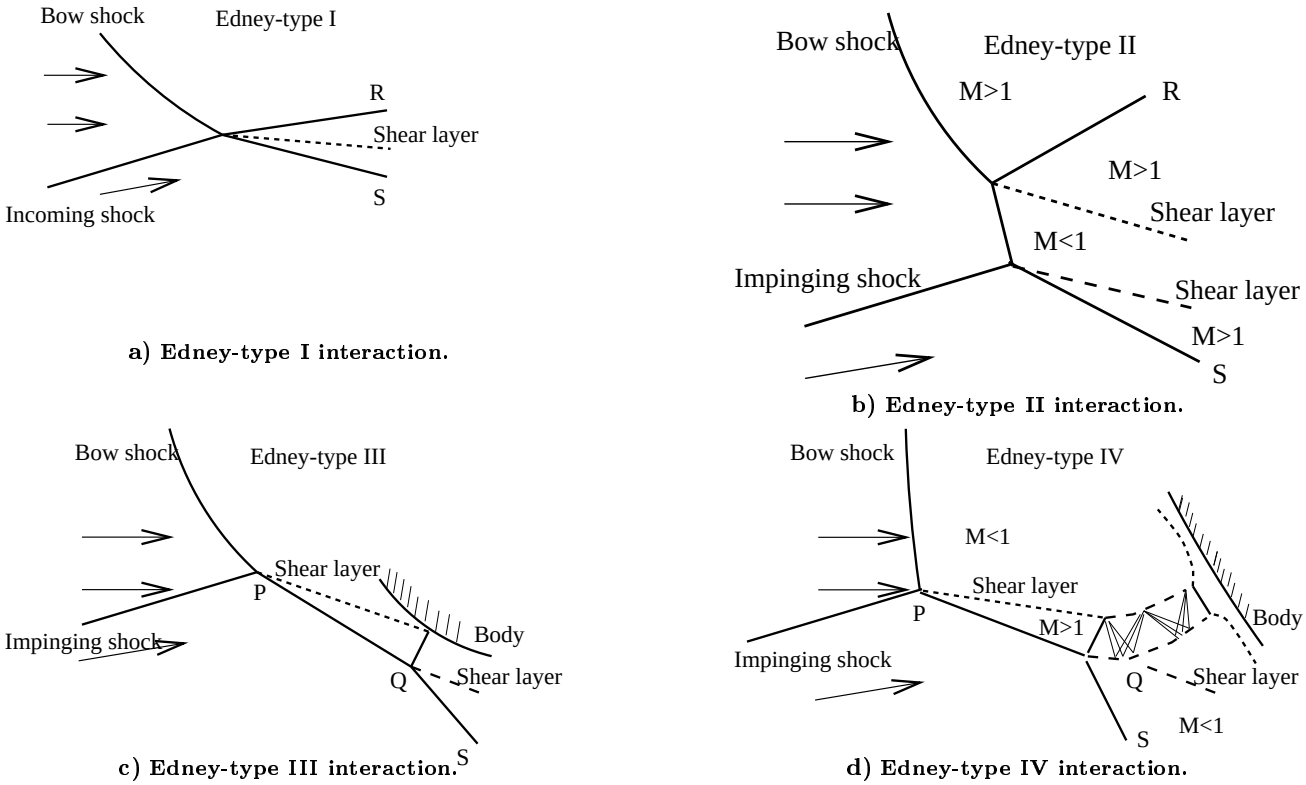

a) Edney-type I interaction.

b) Edney-type II interaction.

c) Edney-type III interaction.

d) Edney-type IV interaction.

Fig. 3 Sketches of the Edney-type I-II-III and IV interactions.

NUMERICAL METHOD

The computational results that will be presented in this paper have been obtained using a well established numerical technique, whose details, which will be not described here, can be found, for instance, in references,[9].[10] In synthesis, the Navier-Stokes equations for two-dimensional flows are solved. The numerical method adopts a finite volume discretization of the physical domain, an explicit integration scheme, a flux difference splitting technique[11] for the evaluation of the convective fluxes and a standard cell centered method for the diffusive fluxes. A multi-block domain decomposition method is used, that allows for an efficient distribution of grid points across the computational domain. Finally, a nominal second order accuracy in space and time is reached using an Essentially Non-Oscillatory scheme.[12]

FLOWFIELD FEATURES

Depending on the strength of both the impinging and the bow shocks and on their relative positions, various shock interference patterns can occur. In his fundamental work, Edney[1] classified six types of interactions. The first four interaction patterns are sketched in figure 3 for comparison with the numerical results that will be shown in the next lines and the reader is encouraged to consult the Edney's report for details.

In the following, the results of several numerical tests performed by the author changing the incoming shock position will be shown in order to demonstrate the effect of the various interference patterns on the flowfield and on the wall pressure and heat transfer levels. The freestream conditions and the incoming shock strength are those of the CALSPAN's run 38. The mesh used in such computations is composed of 150 points in the normal direction, with grid stretching close to the wall. In the tangential direction, the grid spacing is 1 degree in the range $[-40^o : +40^o]$. Then, the tangential grid spacing increases linearly up to a maximum value of 1.5 degrees at the upper and lower boundaries. The Mach number contours and the streamlines patterns are shown in figure 4 for twelve different shock positions. In the case of the first shock position (#1) an Edney-type IV interaction occurs, but the resulting supersonic jet does not impinge on the cylinder wall. The stagnation point is very close to the symmetry axis, but, as it will be shown later, the pressure and heat flux peak values are higher with respect to the undisturbed cylinder, since the stagnation streamline comes from the high pressure side of the impinging shock wave. Lowering the incoming shock position (#2 to #8), the supersonic jet is directed towards the body surface and the flow experiences a final strong compression across a normal shock at a short distance from the wall. Lowering the shock a little more (#9), the slip surface grazes the wall and the normal shock in front of the body disappears. This is an Edney-type III interaction. If we continue to move the incoming shock downwards (#10 and #11), we would expect to see an Edney-type II interaction. In these particular two cases, however, the

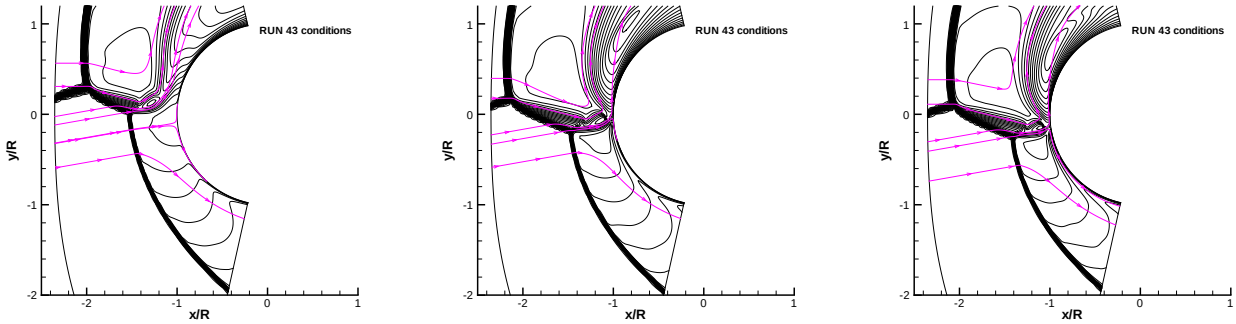

a) Incoming shock position #1. b) Incoming shock position #2. c) Incoming shock position #3.

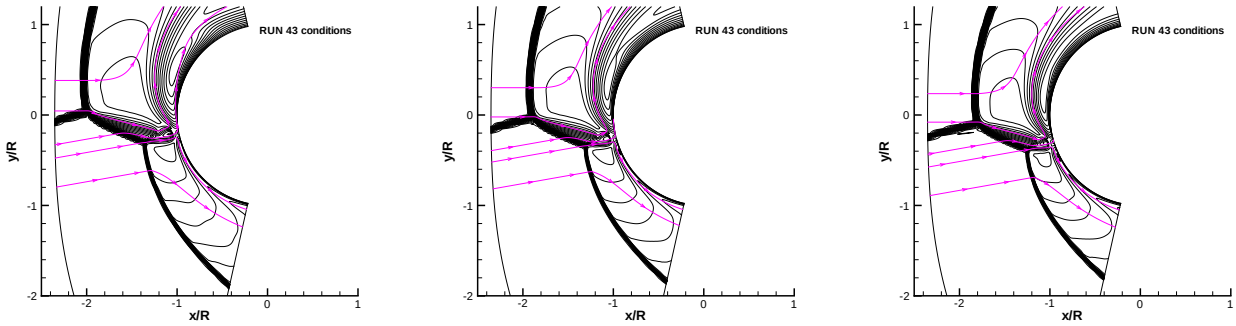

d) Incoming shock position #4. e) Incoming shock position #5. f) Incoming shock position #6.

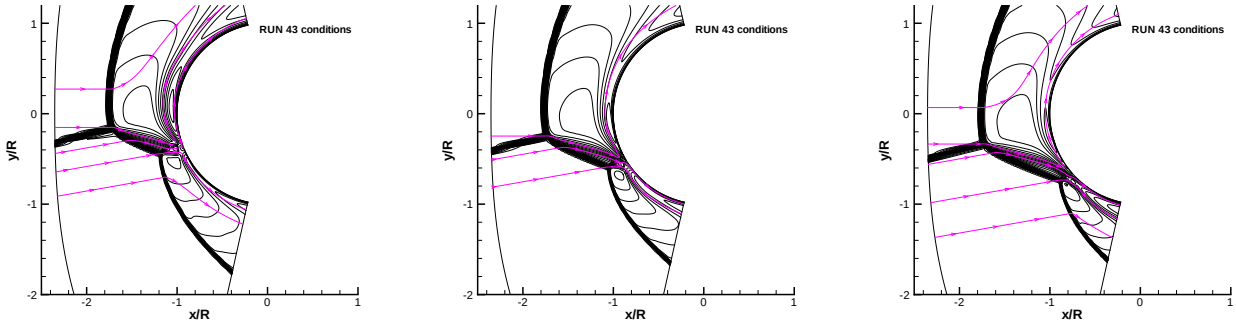

g) Incoming shock position #7. h) Incoming shock position #8. i) Incoming shock position #9.

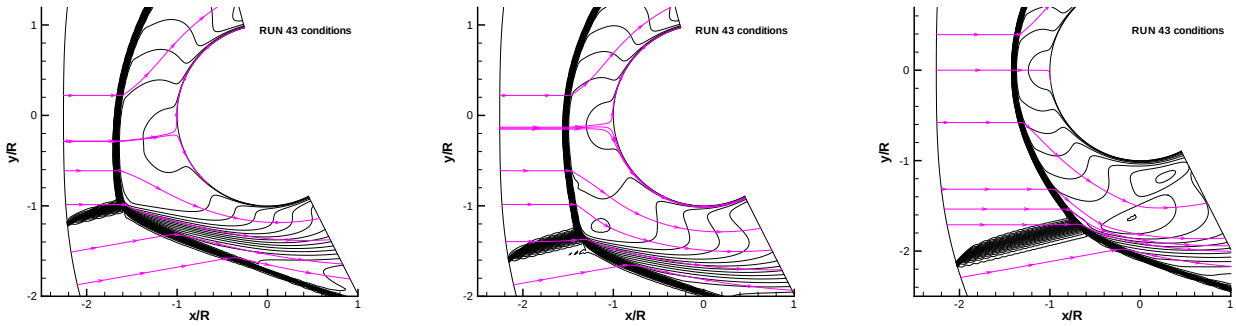

j) Incoming shock position #10. k) Incoming shock position #11. l) Incoming shock position #12.

Fig. 4 Effect of the impinging shock position. Conditions of CALSPaN's RUN 43. Mach number contours.

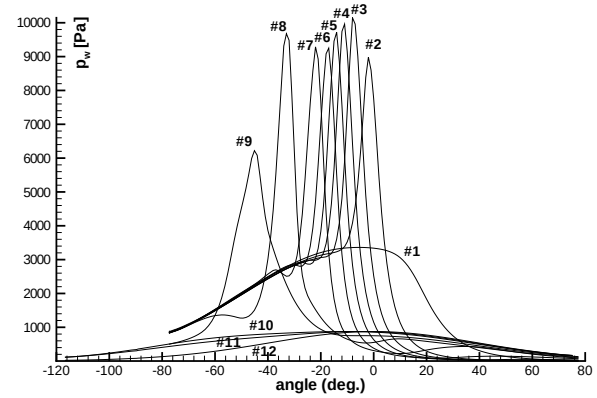

a) Pressure at the wall.

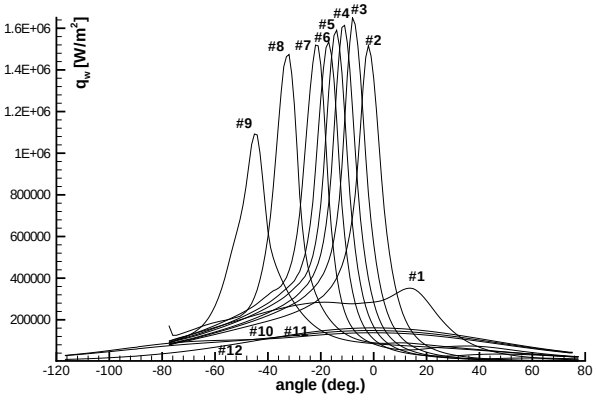

b) Heat flux at the wall.

Fig. 5 Pressure and heat flux at the wall for different incoming shock positions. Conditions of the CALSPAN's run 43.

reflected shock R interacts with the subsonic pocket on the cylinder nose and the Edney-type II interaction is not possible. Finally, an even lower impinging shock (#12) produces and Edney-type I interaction. Pressure and heat transfer levels at the wall for all the twelve situations are shown in figure 5a and 5b. The Edney-type IV interaction clearly produces the highest peak levels, in particular when the jet is directed towards the cylinder and the normal shock is present in front of the body. The highest pressure levels are related to condition #3 and #8, which correspond to a situation when the stagnation streamline crosses the final normal shock respectively at its upper and lower ends, where it is less intense.

RESULTS

Numerical simulation of the ONERA experiments

The experiment conducted at the ONERA concerning the Edney type IV interaction has been replicated with a numerical simulation using the freestream conditions listed in table 3. In predicting this experiment,

Table 3 Numerical freestream conditions for simulating the ONERA experiment.

p_∞	=	5.9	Pa
M_∞	=	9.95	
U_∞	=	1450	m/s
T_∞	=	52.5	K
ρ_∞	=	$3.910 \cdot 10^{-4}$	kg/m^3
μ_∞	=	$3.405 \cdot 10^{-6}$	Pa·s
Re_∞	=	$1.66 \cdot 10^5$	
R_{cyl}	=	0.008	m

a particular care must be employed in correctly simulating the flow about the shock generator also. In fact, due to the model set-up used (figure 1), an intense expansion is generated at the corner between the upstream part of the shock generator, which is a wedge, and the second part, which is a flat plate. The expansion fan bends the oblique shock wave and makes the flow in high-pressure side of it not uniform. In addition to this, the smallness of the cylinder radius with respect to the shock generator characteristic length implies that a slight variation of the inclination (or position) of the impinging shock may produce a noticeable displacement in the position of the stagnation point. Therefore, for validation purposes, it is necessary to numerically reproduce with great accuracy the flow about the shock generator.

Computations have been performed using one grid for the upper part of the shock generator, one grid for the lower part, one grid for the stream past the shock generator and finally a grid composed of 300x351 points in the normal and tangential directions, respectively, for the cylinder. All the grids are stretched in the normal direction close to the solid walls. The mesh around the cylinder is refined with stretching also in the region of the supersonic jet. The external boundaries of the four grids used are visible in figure 6.

In order to estimate the scale of the grid cells in relation with flow conditions, the dimensionless distance from the wall y^+ of the first cell centers has been computed. The plot, not included here for lack of space, shows that first cells centers lay at distances $y^+ \leq 0.2$ for most part of the cylinder walls, and reach the maximum value of 0.74 in correspondence with the stagnation point. Thanks to this analysis and to preliminary investigations with coarser grids, we are confident that the grid convergence has been reached.

In this particular test case, the intersection between the incident oblique shock generated by the wedge and the detached shock which forms ahead of the cylinder takes place where the bow shock is strong (subsonic flow in the high pressure side). The interaction belongs to the Edney-type IV family[1] and is characterized by the presence of a supersonic jet surrounded by subsonic flow. In principle, a repeated pattern of expansions and compressions develops inside the jet channel, but in this case, due to the vicinity of the jet to the cylinder

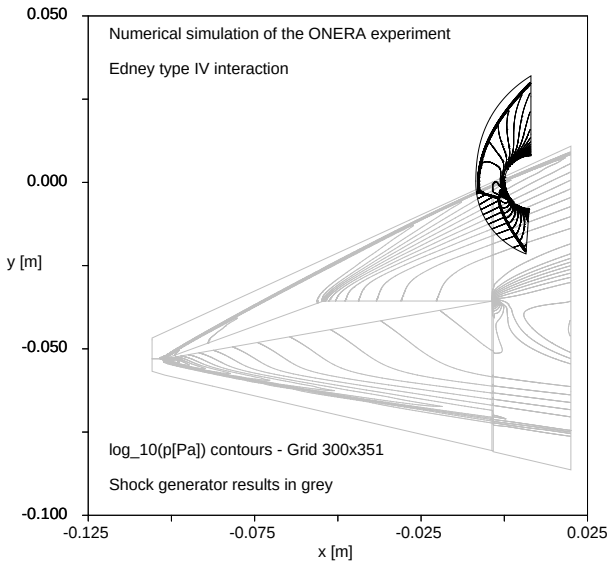

a) Log_10 of pressure contours.

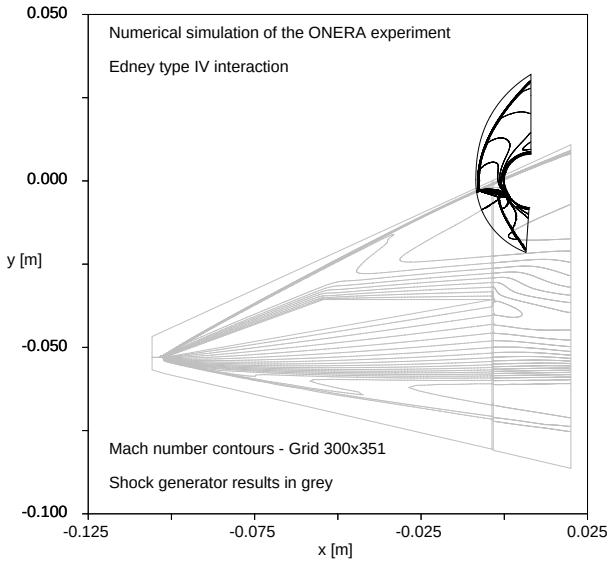

b) Mach number contours.

Fig. 6 Simulation of the complete flowfield for the ONERA experiment.

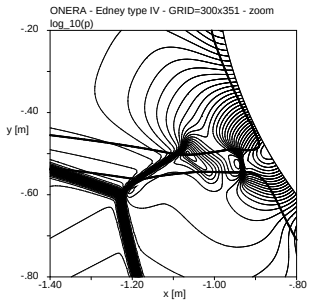

a) Log_{10} of pressure contours.

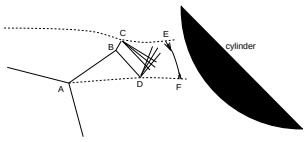

b) Wave pattern inside the jet.

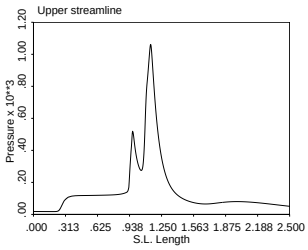

c) Pressure variation along the upper streamline.

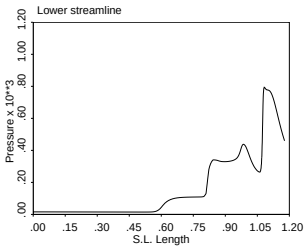

d) Pressure variation along the lower streamline.

Fig. 7 Investigation of the wave pattern inside the supersonic jet.

wall, we can distinguish only a few of them. In particular, from the analysis of our results, we interpret the flowfield inside the jet as sketched in figure 7b). The shock wave at the "entrance" the supersonic channel is irregularly reflected from the upper slip line and forms a λ-shock. In correspondence with the reflection point, an expansion fan forms to permit to part of the streamlines to flow slightly upwards. At the opposite side of the jet, the second leg of the *lambda*-shock interacts with the lower slip line and is reflected as an expansion fan, which deviates part of the jet slightly downwards. Approaching the body, the supersonic stream which flows inside the jet is suddenly decelerated through a detached shock. The jet is finally divided in two streams which flow upward and downward the stagnation point. The previous interpretation arise from the study of figure 7, where log_{10} of pressure plots are shown in part a), with the paths of two streamlines superimposed. In figures 7c) and 7d), the pressure conditions along these streamlines are displayed. It can be noticed that, after the pressure rise due to the oblique Mach shock, a second increase in pressure, due to the shock at the "entrance" of the channel, is present. This second pressure rise is stronger and unique for the upper streamline, which crosses the λ-shock practically at the triple point, while it is less intense, and followed by a second compression for the lower streamline, which crosses the two legs of the λ-shock. Then, both streamlines experience a pressure drop due to the expansions fans and finally a strong compression through the detached shock in front of the body. This last pressure rise is smoother for the upper streamline than for the lower one, because the former crosses the detached shock at its margins, where it is just starting to appear, created by converging compression waves.

A larger scale view of the interaction is shown in figure 8. Notice that the position of the cylinder bow shock is completely different with respect to the undisturbed case, being the shock layer thickness of the upper portion more than doubled.

Computed pressure and heat flux distributions at the wall are shown in figure 9, where they are also compared with results of experiments conducted in the ONERA R5Ch low density wind tunnel.[4] The com-

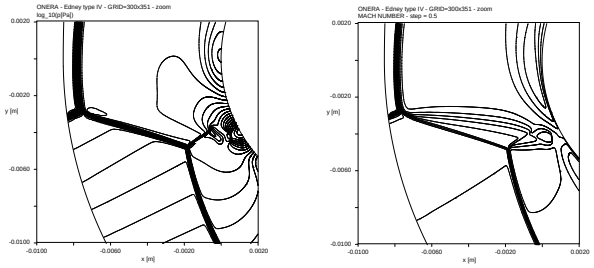

a) Log_{10} of pressure contours. b) Mach number contours.

Fig. 8 The interaction region.

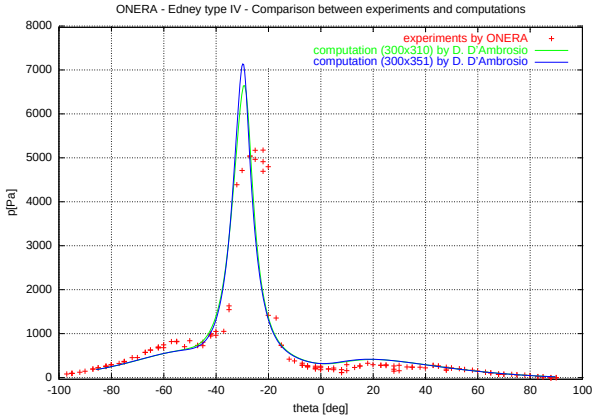

a) Wall pressure distribution.

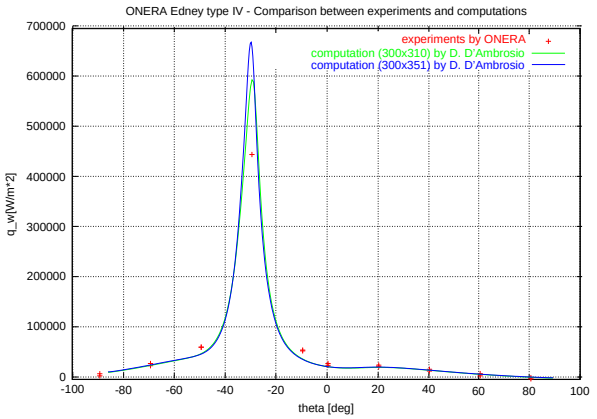

b) Surface heat transfer distribution.

Fig. 9 Pressure and heat flux distribution at the wall. Experimental values versus numerical predictions.

parison appears to be rather good. Concerning the level of the pressure peak, we explain the higher value displayed by the numerical simulation with the bad spatial resolution of the experiments, due to the fact that in the latter the diameter of the pressure holes is rather large (1.5 mm).[13] The situation is improved for the heat fluxes, since the diameter of the thermocouples is smaller (0.4 mm).

In order to simulating the effect of the dimension of the pressure taps and of the thermocouples on the results, the numerical data have been averaged out

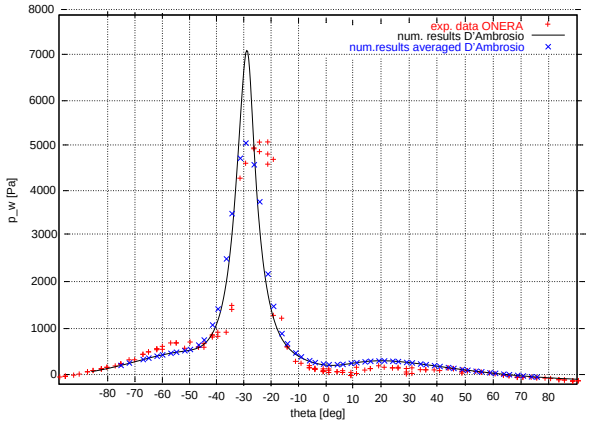

a) Wall pressure distribution.

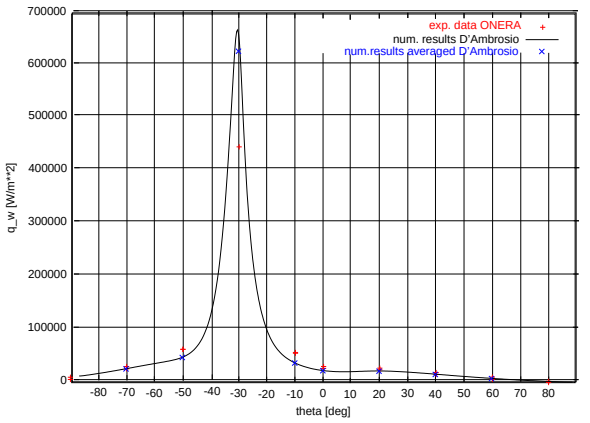

b) Surface heat transfer distribution.

Fig. 10 Pressure and heat flux distribution at the wall. Experimental values versus averaged and not averaged numerical predictions.

around every experimental measurement point considering a pressure tap with a 1.5 mm diameter and a thermocouple with a 0.4 mm diameter. For the pressure taps, this results in averaging out across a circumferential angle of $\pm 5.37^o$ with respect to the nominal measurement point. A weighted average has been done to keep into account the stretching of the grid in the tangential direction. The results obtained for the surface pressure distribution are very interesting (figure 10). In fact, one can see that the peak level is the same when comparing experiments and (averaged) numerical predictions. The improvement is definitely less important when observing the surface heat flux distribution, but in this case the experimental data are few, and it is impossible to decide whether the largest experimental is the real peak or not.

Numerical simulation of the CALSPAN experiments

In this section, numerical results related to RUN 38 and RUN 43 will be shown and compared with the experimental data. The conditions for the two test cases are listed in table 2. For both cases the correct incoming shock position to match with the experiments was

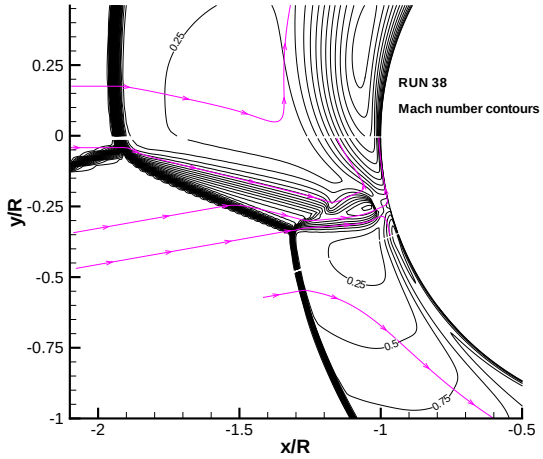

a) Mach number contours.

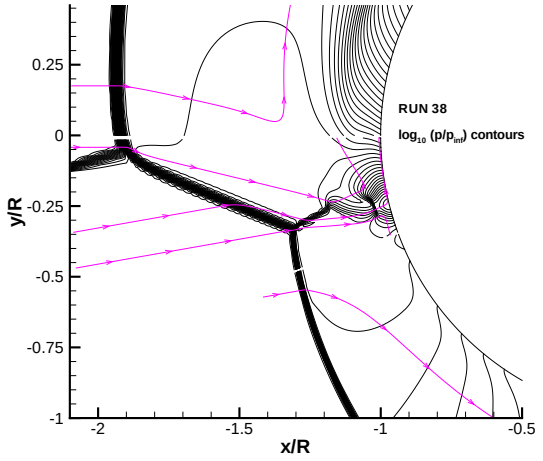

b) Surface heat transfer distribution.

Fig. 11 Mach number and $\log_{10}$ of pressure for RUN 38.

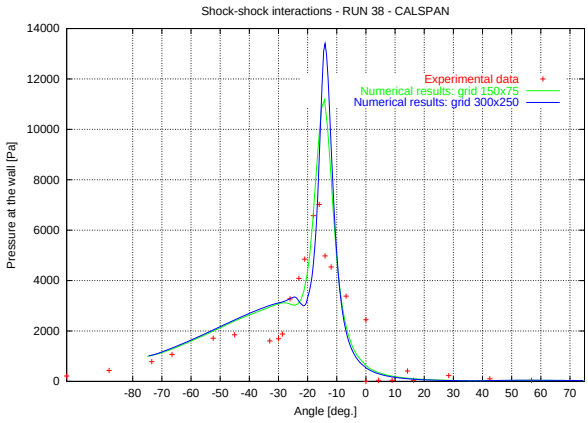

a) Surface pressure distribution.

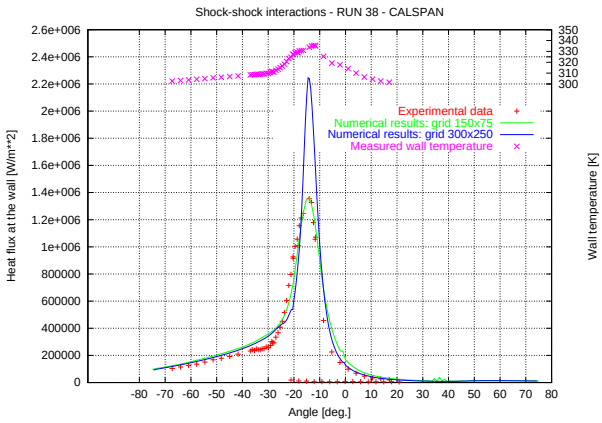

b) Surface heat transfer distribution.

Fig. 12 Pressure and heat flux distribution at the wall for RUN 38. Experimental values versus numerical predictions.

obtained moving the shock until the wall pressure and heat flux peaks were in the same tangential position of the experimental data.

Concerning RUN 38, the computations were performed using two different grids. The coarser grid is composed of 150 points in the normal direction, with a constant spacing of 1 degree in the tangential direction. The finer mesh has 300 points normal to the wall and the constant tangential spacing is 0.5 degrees. The resulting configuration is an Edney-type IV interaction, as it is evident from figures 11a and 11b. The effect of the grid refinement on the wall pressure and heat flux is shown in figures 12a and 12b, where also the experimental data are plotted. As it typically happens in the numerical simulation of this kind of flows, refining the mesh increases the peak levels. The reason for such a behaviour is not clear, but again it could be ascribed to the finite dimensions of pressure taps and of the thermocouples. In addition to the discrepancy in the peak values, a second disagreement between experiments and numerical results is present in the range between -30^o and -50^o. However, numerical simulations performed by other authors for the same test case are in very good agreement with the present numerical data. One possible explanation for the difference with the experiment could be attributed to some unsteadiness in the incoming shock position during the experimental tests.

The numerical simulation of the experimental conditions of RUN 43 were performed using three different grids. The coarser grid is the one used for investigating the effect of the incoming shock position and is composed of 150 points in the normal direction, with grid stretching close to the wall. In the tangential direction, the grid spacing is 1 degree in the range $[-40^o : +40^o]$. Then, the tangential grid spacing increases linearly up to a maximum value of 1.5 degrees at the upper and lower boundaries, so that the grid dimension is 150x143 points. A second mesh still contains 150 points in the normal direction, but the tangential spac-

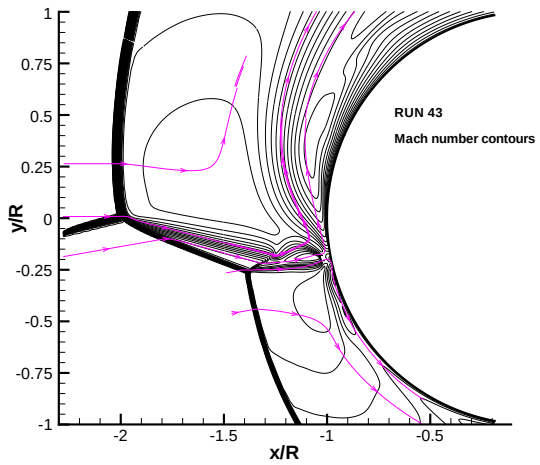

a) Mach number contours.

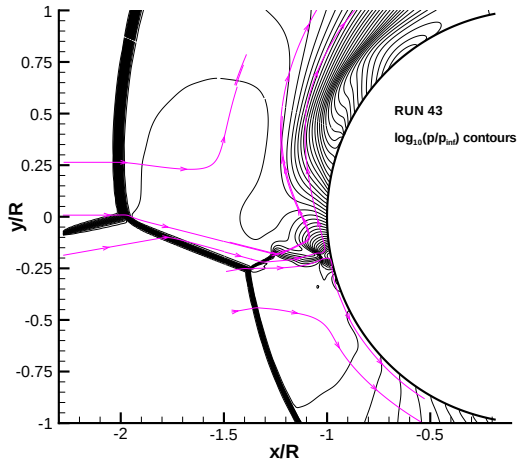

b) Surface heat transfer distribution.

Fig. 13 Mach number and $\log_{10}$ of pressure for RUN 43.

ing in the range $[-40^o : +40^o]$ is now 0.5 degrees, with maximum amplitude of 1 degree at the ends of the computational domain (150x263 points). For the finer grid, 300 points (with stretching) where used in the normal direction, while the tangential spacing is 0.25 degrees between $[-40^o : +40^o]$ and the maximum tangential spacing is 0.5 degrees (300x528 points).

RUN 43 belongs to the family of the Edney-type IV configurations also. The Mach number and $\log_{10}$ of pressure contours shown in figures 13a and 13b clearly reveal the presence of a supersonic jet directed towards the cylinder wall and of a normal shock that decelerates the flow before it reaches the body.

A comparison with the pressure and the heat transfer at the wall measured in the experiments is displayed in figures 14a and 14b. Again the effect of the grid refinement is such that a finer grid produces a higher peak. The comparison with the experiments is not satisfactory as far as the peak values are concerned. Also in this case, it is possible to notice a second discrepancy in the range $[-20^o : -50^o]$. The finer grid shows the trend to get closer to the experimental data in that area, arising the question whether a further grid refinement would be necessary to capture a local physical phenomenon. However, the question about the steadiness of the experiment remains open.

As mentioned in a previous section, in the experiments conducted at CALSPAN it was preferred to use models with non-conducting surfaces. Then, in those cases where the resulting wall temperature rises were important, the surface temperature distribution was tabulated together with the heat transfer rate,

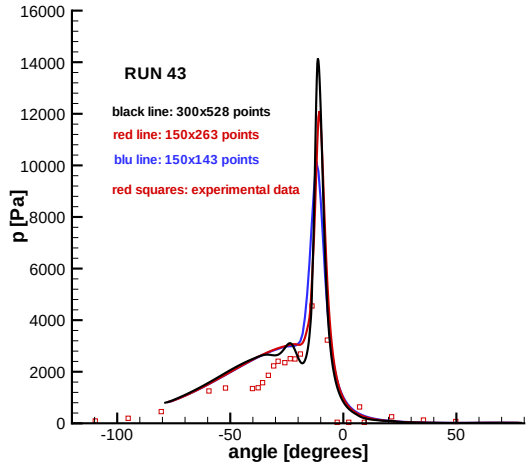

a) Surface pressure distribution.

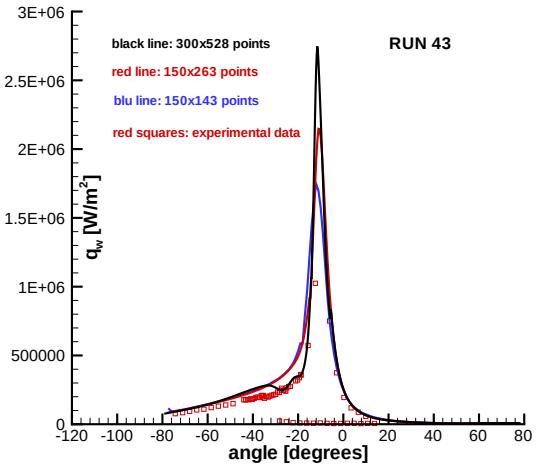

b) Surface heat transfer distribution.

Fig. 14 Pressure and heat flux distribution at the wall for RUN 43. Experimental values versus numerical predictions.

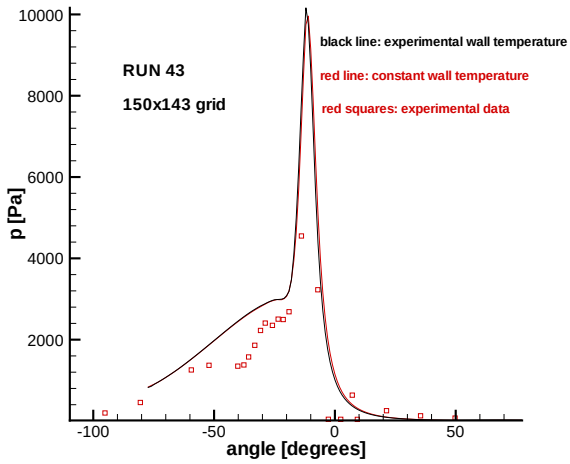

a) Surface pressure distribution.

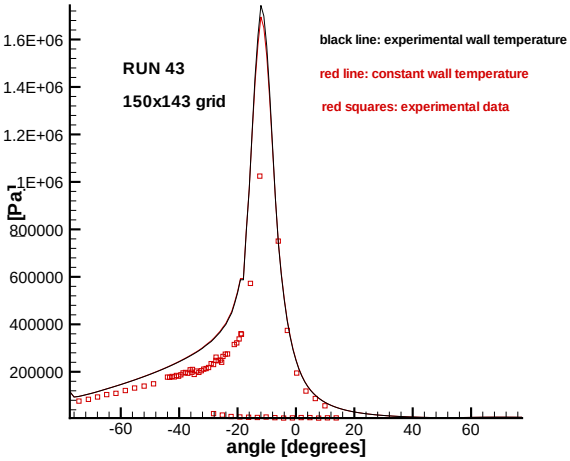

b) Surface heat transfer distribution.

Fig. 15 Pressure and heat flux distribution at the wall for RUN 43 using a constant wall temperature of 300 K or the wall temperature measure in the experiments.

so that it could be used in future numerical predictions as a boundary condition. In order to reproducing at the best the experimental conditions, the numerical simulations were conducted using the wall temperature measured in the experiments as a boundary condition. However, a comparison between two computations performed using the coarser grid with and without the variable wall temperature condition showed that the effect is negligible, as shown in figure 15.

CONCLUSIONS

Computational Fluid Dynamics is a very useful tool for simulating shock-shock interactions, since it consents to predict the heat loads on the body surface for different impinging shock positions. Nevertheless, computations are very sensitive to the grid refinement and it is very difficult to obtain grid convergence in the area where the wall pressure and the heat flux reach their maximum values. In most coditions, the peak levels measured in the experiments are smaller with respect to the numerical predictions. This is a very critical point, since the estimation of the highest heat flux is fundamental for the design of hypersonic vehicles. Further accurate experimental and numerical investigations should be necessary in order to clarify such an issue.

References

[1]Edney, B., "Anomalous Heat-Transfer and Pressure Distributions on Blunt Bodies at Hypersonic Speeds in the Presence of an Impinging Shock," FFA Rept. 116, Aeronautical Research Inst. of Sweden, Stockholm, Sweden, February 1968.

[2]Pot, T., Chanetz, B., Lefebvre, M., and Bouchardy, P., "Fundamental Study of Shock-Shock Interference in Low Density Flow: Flowfield Measurements by DLCARS," *21st Conference on Rarefied Gas Dynamics*, Marseille, France, July 26-31 1998.

[3]Holden, M., Sweet, S., Kolly, J., and Smolinsky, G., "A Review of the Aerothermal Characteristics of Laminar, Transitional and Turbulent Shock/Shock Interaction Regions in Hypersonic Flows," *36th Aerospace Sciences Meeting and Exhibit*, RENO, NV, USA, January 12-15 1998, AIAA Paper 98-0899.

[4]Moss, J., Pot, T., Chanetz, B., and Lefebvre, M., "DSMC simulation of shock/shock interactions: emphasis on type IV interactions," *22nd International Symposium on Shock Waves*, London, Great Britain, July 18-23 1999.

[5]Glass, C., "Numerical Simulation of Low-Density Shock-Wave Interactions," *22nd International Symposium on Shock Waves*, London, Great Britain, July 18-23 1999, also NASA/TM-1999-209358, July 1999.

[6]*East-West High Speed Flow Field Database Workshop*, Vieweg Series: Notes on Numerical Fluid Mechanics, 1998.

[7]Knight, D. D., "Stage I Report," Tech. rep., RTO Working Group 10 "Technologies for Propelled Hypersonic Flight", Subgroup 3 "CFD Validation for Hypersonic Flight", January 2000.

[8]Holden, M., Moselle, J., and Martin, S., "A Database for Aerothermal Measurements in Hypersonic Flow for CFD Validation," Norfolk, VA, USA, 1996, AIAA Paper 96-4597.

[9]D'Ambrosio, D. and Pandolfi, M., "Contribution to Problem T1-97.1: Hyperboloid-Flare (cold)," *First US-Europe High Speed Flow Field Database Workshop - Part II*, edited by S. Borrelli et al., CIRA, AIAA, Naples, Italy, 12-14 November 1997.

[10]D'Ambrosio, D. and Pandolfi, M., "Contribution to Problem T2-97: Hollow cylinder-Flare," *First US-Europe High Speed Flow Field Database Workshop - Part II*, edited by S. Borrelli et al., CIRA, AIAA, Naples, Italy, 12-14 November 1997.

[11]Pandolfi, M., "A Contribution to the Numerical Prediction of Unsteady Flows," *AIAA Journal*, Vol. 22, No. 5, 1983.

[12]Harten, A., Engquist, B., Osher, S., and Chakravarthy, S. R., "Uniformly High Order Accurate Essentially Non-Oscillatory Schemes, III," *Journal of Computational Physics*, Vol. 71, 1987.

[13]Pot, T., November 1998, private communication.